

WILEY-VCH

Implantable, Biodegradable, and Wireless Triboelectric Devices for Cancer Therapy Through
Disrupting Microtubule and Actins Dynamics

Shuncheng Yao, Shaobo Wang, Minjia Zheng, Zhuo Wang, Zhirong Liu, Zhong Lin Wang*,
Linlin Li*

S. Yao, S. Wang, M. Zheng, Z. Wang, Z. Liu, Prof. Z. L. Wang, Prof. L. Li

Beijing Institute of Nanoenergy and Nanosystems

Chinese Academy of Sciences, Beijing 101400, P. R. China.

E-mail: zhong.wang@mse.gatech.edu, lilinlin@binn.cas.cn

S. Yao, Z. Liu, Prof. Z. Li, Prof. Z. L. Wang, Prof. L. Li

School of Nanoscience and Technology

University of Chinese Academy of Sciences, Beijing 101400, P. R. China.

This article has been accepted for publication and undergone full peer review but has not been through the copyediting, typesetting, pagination and proofreading process, which may lead to differences between this version and the [Version of Record](#). Please cite this article as [doi: 10.1002/adma.202303962](https://doi.org/10.1002/adma.202303962).

This article is protected by copyright. All rights reserved.

S. Wang, M. Zheng, Prof. Z. Li, Prof. Z. L. Wang, Prof. L. Li

Center on Nanoenergy Research, Guangxi University, Nanning, 530004, China

Prof. Z. L. Wang

School of Materials Science and Engineering, Georgia Institute of Technology, Atlanta, GA
30332-0245, USA

Keywords: triboelectric devices, cancer therapy, electric field stimulation, biodegradable, mitosis

Electric field-based stimulation is emerging as a new cancer therapeutic modality through interfering with cell mitosis. To address its limitations of complicated wire connections, bulky devices, and coarse spatial resolution, we propose an improved and alternative method for wirelessly delivering electrical stimulation into tumor tissues through designing an implantable, biodegradable and wirelessly controlled therapeutic triboelectric nanogenerator (ET-TENG). With the excitation of ultrasound (US) to the ET-TENG, the implanted ET-TENG can generate an alternating current voltage and concurrently release the loaded

This article is protected by copyright. All rights reserved.

anti-mitotic drugs into tumor tissues, which synergistically disrupts the assembly of microtubules and filament actins, induces cell cycle arrest, and finally enhances cell death. With the assistance of US, the device can be completely degraded after the therapy, getting free of a secondary surgical extraction. The device can not only work around those unresectable tumors, but also provides a new application of wireless electric field in cancer therapy.

1. Introduction

In mammalian cells, mitosis progression and chromosome segregation into daughter cells are accurately guided by assembly of a bipolar microtubule-based spindle under the strict surveillance of spindle assembly checkpoint signaling^[1]. Disruption of microtubule dynamics induces prolonged mitotic arrest and eventually cell apoptosis^[2]. Anti-mitotic drugs that target dynamic microtubule assembly are clinical mainstays of anti-cancer chemotherapy^[3]. These drugs, whether microtubule-stabilizing or microtubule-destabilizing agents, can bind to tubulin, disrupt microtubule dynamics, delay mitotic progression, and finally trigger DNA damage and apoptosis. However, in clinic applications, these drugs bring severe toxicity including liver damage, acute allergic reactions, hypotension, and thrombocytopenia.

This article is protected by copyright. All rights reserved.

Moreover, the development of drug resistance against these drugs is frequent that limits their clinical effectiveness.

Microtubules are assembled by electrically polar tubulin sub-units and have large electric dipole moments^[3a], thereby can be disoriented by the forces of electric fields. Based on this foundation, tumor treatment fields (TTFields) as a unique and non-invasive tumor treatment modality have been developed and rested on for improving cancer therapy. TTFields utilize alternating electric fields in the medium frequency range (10 kHz - 1 MHz) to disrupt the proliferation of cancer cells by interfering with the assembly and directionality of mitosis-associated proteins, especially tubulin^[4]. This new electrotherapy has been proved to be lesser toxic and has comparable efficacy to chemotherapy, improving the quality of patient life^[5]. However, TTFields still suffers from disadvantages of complicated wire connections, bulky devices, coarse spatial resolution, and risk factors to patients including skin erosion, severe contact dermatitis, and skin infection^[6]. In addition, its electric field is remotely delivered to cancer cells via insulated electrodes attached to skin, which would be largely attenuated into tumors especially those deep-seated in body^[7]. For efficient therapy, least 18 hours every day is required for this electrical stimulation.

This article is protected by copyright. All rights reserved.

Recently, implantable biomedical devices (IBDs) (*e.g.*, sensors, cardiac pacemakers, and nerve, brain, and bone stimulators) are under high-speed growth stage that open new era of intelligent therapy. As long as the difficulty in energy supply is resolved, IBDs are expected to face the above dilemmas of TFields^[8]. Thriving in this decade, triboelectric nanogenerators (TENGs) that can efficiently convert mechanical energy into electrical signals have been directly applied for safe electrical stimulation without obvious side effects on bodies^[9]. Specifically, those flexible and implantable TENGs can harvest tiny biomechanical energies from the heart, lungs, chest, or muscles in bodies^[10] to drive the IBDs^[11], realizing a self-powered actuation. Therefore, we expect the implantable TENG can function as ideal energy supply for realizing electrical stimulation therapy of cancer. Additionally, for cancer therapy, it is also expected that the implantable devices with temporary therapeutic purposes can be wirelessly manipulated and biodegraded to avoid the secondary surgical extraction and infection risk^[12].

In this work, we design an implantable, biodegradable, and external US-activated cancer therapeutic device made of drug loaded therapeutic TENG (ET-TENG) for synergistic disrupting of microtubule dynamics and cell mitosis. The flexible and ultrathin ET-TENG device serves as a power output device, and can release drugs to synergize the electrical

This article is protected by copyright. All rights reserved.

stimulation^[13] (Figure 1). Ultrasound not only provides wireless activation to ET-TENG for locally producing electrical stimulation, but also regulates the biodegradation of ET-TENG^[8a, 12c, 14]. We demonstrate that the treatment device ET-TENG can be completely degradable in the animals after completing the therapy under US activation and does not induce any long-term adverse effects. Notably, the treatment device requires only a short treatment time (within 90 min) and a single treatment to achieve the efficient suppression of a wide range of tumors, which is a novel tumor treatment modality based on wireless electric field in combination with conventional chemotherapy. This work opens up a new avenue for designing implantable device that can enhance cancer therapy.

2. Results and discussion

2.1 Fabrication and performance of the ET-TENG device

We first fabricated the US-activated ET-TENG device through directly immobilizing the drug loaded nanoparticles onto the ultrafine and flexible TENG. Figure 2A shows the conceptual diagram and optical photographs of the device. As the electricity-generation unit of ET-TENG responsive to external US, the thin-film contact-separation mode TENG (dimensions of 1 cm×1 cm, total thickness of ~130 μm) consists of two separate films

This article is protected by copyright. All rights reserved.

sandwiched by air; each integrated film has two constitution layers (Figure 2A). To form the upper composite film, a ~100 nm ultrathin Mg layer serving as the back electrode was deposited on a ~ 60 μm poly (ϵ -caprolactone) (PCL) nanofibrous film that was doped with hollow structured covalent organic framework nanocage (hCOF) (denoted as PCL-hCOF)^[15]; and another Mg layer serving as the triboelectric layer was deposited on the pure PCL nanofibrous layer to form the lower composite film. This PCL layer mainly plays a role of waterproof, ensuring the stable output of the TENG when being implanted into body. The two separate films were assembled together by hot pressing at their peripheral areas to form an integrated structure, between which an air spacer was introduced, allowing for physical contact/separation and contact electrification under external ultrasonic mechanical waves. Subsequently, ET-TENG can be facily acquired by directly spraying the drug loaded nanoparticles onto TENG (Figure 2A).

For realizing efficient drug loading and electricity-responsive drug release, we selected carbonaceous metal organic framework zeolitic imidazolate framework-8 (ZIF-8) nanoparticles (denoted as CZIF) as the drug carrier (Supplementary Figure 1). CZIF has an approximately identical morphology with that of ZIF-8 with slightly shrunken size (Figure 2B, Supplementary Figure 2). It has a high Brunauer-Emmett-Teller (BET) surface area of

This article is protected by copyright. All rights reserved.

543.97 m² g⁻¹ and mesoporous pores with average size of 2.2 nm, favorable for drug loading via physical absorption and electrostatic interaction (Figure 2C, Supplementary Figure 3). After docetaxel (DTX) loading with a drug loading amount of 13.4%, the resultant CZIF-D displays characteristic absorption peaks at 1712.9 cm⁻¹ and 1637.8 cm⁻¹ contributed from DTX in the Fourier transform infrared (FT-IR) spectrum (Supplementary Figure 4). The morphology, hydrodynamic size (~140 nm), and dispersibility in aqueous solution (reflexed by polydispersity index) of the nanoparticles have no obvious change after DTX loading (Supplementary Figure 5).

The working mechanism of ET-TENG under ultrasonic mechanical waves is shown in Figure 2D. When US is imposed to transmit mechanical vibrations, the ultrathin and flexible TENG undergoes periodic and inter-layers contact-separation, and the frequency of contact-separation synchronizes with that of US. When an ultrasound wave comes, the upper Mg triboelectric layer deforms and comes in contact with the lower PCL-COF layer, and positive and negative polarities are generated on the Mg and PCL-COF layers, respectively, through contact electrification. The positive charges accumulated on the Mg film effectively shield the negative charges on the PCL-COF layer. When the Mg layer moves away from the PCL-COF layer, the accumulated negative charges can be released into the surrounding

This article is protected by copyright. All rights reserved.

environment (*i.e.* tumor tissues) through the other Mg electrode layer that faces outwards. In this way, the accumulated charge moves back and forth to produce a continuous alternating current (AC) voltage. The AC voltage further imposes on CZIF-D to stimulate drug release into the tissues. The electrostatic distribution during a working cycle was confirmed by finite element analysis (Supplementary Figure 13).

It deserves mentioning that for optimizing the output performance of TENG, we incorporated hCOF^[15] into the triboelectric PCL layer to improve its surface potential. From the Kelvin probe force microscopy (KPFM) measurements (Figure 2E), the pure PCL fibrous film shows a surface potential of 167 mV, while the surface potential increases by 94 mV after the hCOF incorporation. It is mainly due to the energy aggregation ability of hCOF with a large number of oxygen-containing groups^[15]. To simulate the realistic application scenario, we sandwiched ET-TENG between two pieces of fresh pork skins with thickness of 2 mm, and imposed US from the top of the skin (Figure 2F). To ensure biosafety, we selected US with a frequency of 23 KHz and a low power intensity of 0.8 W cm⁻² that will not induce thermal and mechanical injury to tissues (Supplementary Figure 14). Under this condition, ET-TENG produced a stable voltage output of 3.26 V with a frequency identical to that of US (Figure 2G, Supplementary Figure 15). Under the same US condition, its output was 1.9-fold

This article is protected by copyright. All rights reserved.

higher than the counterpart without hCOF doping (Figure 2H). As the US power intensities increased, the output of TENG gradually improved and reached 3.92 V at a US power of 2 W cm⁻², while that without hCOF was only slightly increased (Figure 2G, H). Also, we found that variations in ultrasound distance (1, 2, and 4 mm) and tissue types (tumor, muscle and skin) had a slight influence on the TENG output voltages (Supplementary Figure 16-17). We also verified the good biocompatibility of TENG by co-culturing it with mouse fibroblast L929 and NIH-3T3, which didn't induce observable changes in cell morphology (Figure 2I) and viability (Supplementary Figure 17).

Under the stimulus of the US-activated electrostimulation (shorten as E), DTX in CZIF-D located on ET-TENG can be released. The ET-TENG cumulatively released 14.8, 22.8, 34.8, 42.8, and 52.6% of the loaded DTX into surroundings for 1 to 5 cycles of stimulations during 12 h, respectively (US frequency of 23 kHz, one cycle duration of 10 min, and TENG output voltage of 3 V) (Figure 2J). After 24 h, the cumulative DTX release reached 56.9%, remarkably higher than 19.4% of that without E stimulation. We also found that the drug release was voltage-dependent (Supplementary Figure 19). The accelerated drug release was mainly due to the regulation of electrostatic interaction between the drug molecules and CZIF^[15-16].

This article is protected by copyright. All rights reserved.

2.2 *In vitro* cancer therapy

To verify our prediction that the medium-frequency E in combination with DTX can magnify cancer cell killing through disrupting microtubule dynamics and cell mitosis, we investigated the anticancer effect of CZIF-D under E stimulation (CZIF-D + E) at the cellular level (Figure 3A). First, we evaluated the cell killing effect against 4T1 mouse breast cancer cells. The results showed that the cells had over 90% cell survival when only exposure to CZIF or CZIF + E (CZIF incubation followed by E stimulation for 90 min) (Figure 3B). When the cells were treated with DTX (5 nM) and DTX + E (5 nM DTX followed by E stimulation for 90 min), the cell survival rate decreased to 87.7% and 77.5%, respectively. In comparison, treatment of the cells with CZIF-D + E (with equivalent DTX, E stimulation for 90 min) decreased the cell survival to 51.4%. We then evaluated the therapeutic effect against the other cancer cells including mouse melanoma cells (B16f10), human Hela cells, mouse bladder cancer cells (MB49), and rat C6 glioma cells (Figure 3C-F). Although the cells showed viability different to each other, the trends of cell killing effect among different groups were similar, with the sequence of CZIF-D + E > CZIF-D > DTX. Interestingly, we found that the cell survival rate of C6 glioma cells was only 19.2% after the CZIF-D + E

This article is protected by copyright. All rights reserved.

treatment. The half maximal inhibitory concentration (IC_{50}) of DTX against C6 cells was detected to be 11.8 nM (Supplementary Figure 18). In contrast, for the CZIF-D + E treated cells, concentration of DTX inducing about 50% of cell inhibition was only 0.7 nM, decreased by approximate 16.9-fold. The cells killing effects of CZIF-D + E were improved by increasing the concentration of CZIF-D, increasing the electric voltage and prolonging the duration of E stimulation (Figure 3G-I). When the concentration of CZIF-D reached 120 ng/mL with corresponding DTX concentration of 19.9 nM, the cell survival rate of C6 decreased to 6.7% (Figure 3G). When 4 V voltage was applied, the cell survival rate was 8.1% (Figure 3H). And the cell survival rate was 8.9% when the stimulation time lasted for 2.5 h (Figure 3I). These results also indicated that hCOF doping into PCL for improving TENG output favored the cell killing. The live and dead cell staining results were consistent that most of the cells (95.9%) were killed in the CZIF-D + E group (Figure 3J-K).

We also loaded another anti-microtubule drug paclitaxel (PTX) into CZIF (denoted as CZIF-PTX) to detect its synergy with E stimulation. Similar to the outcome of DTX, the survival rate of C6 cells was only 13.9% in the CZIF-PTX + E group (with 4.7 nM PTX) (Figure 3L). It verified that the synergy of anti-microtubule drugs with the E stimulation magnified cancer cell killing. We subsequently evaluated the killing effect of US, US +

This article is protected by copyright. All rights reserved.

PCL-Mg, US + PCL, US + PCL-hCOF and US + PCL-Mg-hCOF on C6 cells to exclude the possible therapeutic effect of US and components of TENG (Figure 3M). After all these treatments, the cell survival rate remained above 90%, ensuring that the *in vivo* implantation of ET-TENG and exogenous US will not cause damage to normal cells.

2.3 Mechanism of cancer cell killing

Both electric field and DTX can interfere with microtubule assembly that are responsible for the formation of bipolar spindle during cell mitosis^[17]. In mammalian cells, microtubule and actin filament that are functionally cross-linked to each other engage in many core biological processes including vesicle transportation, cell migration, polarity, and mitosis, and cancer cell invasion. It was reported that changes in the actin cytoskeleton and microtubules are related to each other and actin filament drives cytokinesis at the final stages of cell division^[18]. To dig the molecular mechanism of the enhanced cell killing effect, we detected the influence of the therapy on microtubule and actin cytoskeleton, and cell mitosis in C6 cells. Before the treatments, the cells were synchronized into their quiescent phase (G₀). The immunofluorescence images showed that after treatment with CZIF-D and DTX + E, β -tubulin expression of the cells decreased to 87.4% and 76.5% of the original level,

This article is protected by copyright. All rights reserved.

respectively (Figure 4A and C). In comparison, CZIF-D + E treatment not only significantly reduced β -tubulin expression to 63.1% of the original level, but also interfered with the aggregation of β -tubulin into bipolar spindle (Figure 4A, Zoom part). Flow cytometry analysis to detect β -tubulin expression gave the similar results (Figure 4D). In addition to the influence on microtubule expression and assembly, CZIF-D + E treatment also disturbed cellular β -actin assembly (Figure 4B). Western blot results showed that after the CZIF-D + E treatment, the expressions of β -tubulin, γ -tubulin and β -actin decreased to the lowest level, representing 22.89%, 78.76% and 34.75% of their original levels, respectively (Figure 4E-F). These results suggested that the combination of CZIF-D and E significantly down-regulated β -, γ -tubulin and β -actin expression and disrupted assembly of microtubule and actin cytoskeleton. During cell mitosis, α - and β -tubulin dimers assemble into canonical tubulin heterodimer and polymerize into microtubules, and γ -tubulin isotype is required for microtubule nucleation to initiate microtubule assembly. The downregulation of their expression and disruption of their functional assembly will undoubtedly disturb cell mitosis and cell division.

To detect the effect on cell division, cell cycle progression was examined. As shown in Figure 4G-H, the proliferative C6 cells without any treatment were mainly in their G_0/G_1

This article is protected by copyright. All rights reserved.

phase (~50.9%) and S phase (~26.7%), and only ~9.91% of the cells were in the G₂/M phase. After CZIF + E, DTX, DTX + E, CZIF-D and CZIF-D + E treatments, the percentage of C6 cells in their G₂/M phase increased to 15.6%, 30.6%, 48.2%, 39.4% and 61.1% of their total, respectively, and cells in the G₀/G₁ phase decreased to about 42.8%, 33.7%, 21.4%, 37.9% and 7.48% of their total, respectively. These results suggested that the E simulation tremendously amplified cell cycle arrest in G₂/M phase, which finally induced cell death.

To further determine the molecular signaling pathways triggered by CZIF-D + E, bulk RNA-sequencing analysis was conducted to compare the cellular transcript levels after various treatments. As a result, the C6 cells had the largest number of up- and down-regulated differentially expressed genes (DEGs) (4162 DEGs from ~19000 genes; 2060 up-regulated and 2102 down-regulated) after the treatment of CZIF-D + E (Figure 5A). The Gene Ontology (GO) term enrichment analysis between the CZIF-D and CZIF-D + E groups revealed that DEGs mainly enriched in organelle damage, nuclear change, protein complex synthesis, apoptosis, and cytoskeletal fraction (Figure 5B). Meanwhile, KEGG pathway enrichment analysis displayed a differential enrichment of signaling pathways associated with apoptosis and mitosis (Figure 5C). For the mitosis pathway (Figure 5D), only *Rasal2* and *Tmbin1* were regulated under E alone. When drug delivery (CZIF-D) synergized

This article is protected by copyright. All rights reserved.

with E stimulation, *Parva*, *Usp5*, *Cdkn1b*, *Zfp207*, *Myh9l1*, and *Rhbdd2* were specifically regulated compared to that of mere CZIF-D treatment. Meanwhile, the expression of *Mtss1*, *Ppp1r9b* and *Ddah2* were specifically regulated under the CZIF-D + E treatment compared to the E treatment. When treatment of the cells with CZIF-D, *Ddx17*, *Mmp14*, *Mcm3*, *Mybl2* and *Ptpn11* were regulated, and *Kifc1* and *Cyp26b1* were downregulated compared with that of E treatment. Therefore, we can conclude that the maximum number of mitosis-related genes were regulated under the synergistic action of CZIF-D and E, resulting in tremendous disruption of cell mitosis.

To explore the specific effects of CZIF-D + E, the volcano plot of CZIF-D vs. CZIF-D + E was depicted (Figure 5E). The regulated genes after the CZIF-D + E treatment relative to CZIF-D were consistent with the differential gene analysis in Figure 5D, and the regulated genes of *Tnip1*, *Kif3b*, *Hsph1*, *Mtmr4* and *Hmox1* were all related to cellular mitotic progression. The hierarchical clustering analysis revealed that the parallel samples within the same group had similar gene expression pattern, and the mitosis-related DEGs were consistent with those in the volcano map (Figure 5F). Subsequently, a directed acyclic graph (DAG) enriched with GO categories was constructed, in which each category served as a node (Figure 5G). For differentially expressed nodes associated with the mitotic cell cycle

This article is protected by copyright. All rights reserved.

progression or microtubule network (marked in red in Figure 5G), *Uba52* is one of the most important genes, which encodes a fusion protein comprising ubiquitin at the N-terminus and ribosomal protein L40 at the C-terminus. It interferes with cell cycle by translocating proteins to proteasomes for degradation or mediating intracellular protein interactions through protein ubiquitination^[19].

2.4 *In vivo* biosafety and biodegradability of ET-TENG

For further *in vivo* cancer therapy, we explored the *in vivo* biosafety and biodegradability of ET-TENG under the US activation. First, we tested the degradation of the ET-TENG under different conditions in simulated body fluids (Supplementary Figure 36). As a result, US stimulation (0.8 W cm⁻², 90 min, one stimulation every 7 days) significantly accelerated the degradation of ET-TENG, with almost complete degradation after 21 days. In contrast, without US stimulation, only slight degradation of ET-TENG occurred after 21 days. We also confirmed that pH change (pH 6.5 and 7.4) had almost negligible effect on ET-TENG degradation. The main components of ET-TENG, PCL and Mg electrode are both intrinsically biodegradable materials. We deduce that several factors may be involved in the US-modulated biodegradation of ET-TENG device. First, the ET-TENG was assembled and

This article is protected by copyright. All rights reserved.

self-encapsulated by hot pressing. The locally strengthened acoustic pressure generated by US stimulation may promote the penetration of fluid into the device, which in turn enhances chemical degradation^[12c]. Second, US may directly cut the covalent bonds and destroy the non-covalent interaction, leading to mechanical decomposition of the device^[20]. Next, ET-TENG was subcutaneously implanted into mice between the subdermal and muscular layers (Figure 6A). From the micro-computed tomography (CT) imaging and the peeled residue of the devices, the device without US activation was partially degraded after 35 days of implantation (Figure 6B); when US was imposed for only once (90 min), ET-TENG was completely degraded after 35 days (Figure 6C). Moreover, the surgical wound healed well and no obvious infection was detected (Figure 6D). Histopathological hematoxylin and eosin (H&E) staining and CD86 immunohistochemical staining display a complete dermal tissue structure and no obvious inflammation surrounding the implanted site. Additional data to confirm the biocompatibility include the normal routine blood indices and blood biochemical indices (Supplementary Figure 34), and low hemolysis (0.47%) (Supplementary Figure 35). The high biocompatibility and biodegradable properties of ET-TENG guarantee safe application, and secondary invasive surgery can be avoided after the implantation and therapy.

This article is protected by copyright. All rights reserved.

2.5 *In vivo* cancer therapy with ET-TENG

We further evaluated the therapeutic effect of ET-TENG on the subcutaneous C6 tumors in BALB/c nude mice (Figure 6E). To differentiate the effect of different variables, we divided the tumor bearing mice into five groups (n=5) including, 1) control group (denoted as G1); 2) US + TENG group (G2), received implantation of TENG and subsequent US activation; 3) ET-TENG group (G3), received implantation of ET-TENG; 4) DTX + US + TENG group (G4), received intratumoral injection of DTX (5 nM), implantation of TENG and subsequent US activation; 5) US + ET-TENG group (G5), received implantation of ET-TENG and subsequent US activation. For the G2-5 groups, TENG or ET-TENG was implanted underneath the subcutaneous tumors, the wounds were sutured, and then US activation (23 kHz, 0.8 W/cm², 90 min) was applied locally for only once (Figure 6F). To detect the output stability of the TENG during the US activation, we implanted the ET-TENG into a tumor-bearing mouse, positioning it underneath the subcutaneous tumor. US stimulation was then imposed for 90 min locally, and then the device was taken out for characterization (Supplementary Figure 39-40). From the photographs, morphology of the device had no obvious change after the 90 min US stimulation. Additionally, we evaluated its output

This article is protected by copyright. All rights reserved.

performance and observed only a slight decrease in output voltages from 3.37 V to 3.02 V. Therefore, during the 90 min *in vivo* therapy, the device can stably output the electrical stimulation. Meanwhile, the electric field generated by ET-TENG can effectively pass through the tissue for the treatment (Supplementary Figure 41). In the following days of the single treatment, the tumors of the mice in the G1-G3 groups grew fast, and several mice in the G1-G3 groups died during the 14th-20th days of the therapy course. In contrast, all the tumors in the G5 group were significantly suppressed (Figure 6G-J). Finally, the treatment with ET-TENG realized a tumor suppression rate of 86.24% (Figure 6J). Hematoxylin and eosin (H&E) staining and Ki67 immunohistochemistry results showed a significant reduction of malignant cells and minimal tumor cell proliferation in this group (Figure 6K).

3. Conclusion

In summary, we design an implantable and biodegradable triboelectric device that can be wirelessly activated by external US to generate AC voltage and release chemodrugs, synergistically disrupting cytoskeleton assembly and cell division and finally improving therapeutic outcome. Compared with those current TTFIELD, our designed device has the main advances includes: 1) The whole device that is ultrathin and mechanically flexible can be

This article is protected by copyright. All rights reserved.

locally implanted into body during the surgical removal of tumor tissues, or around those unresectable tumors to function. The US activation that trigger the generation of electric field and release of drugs is wirelessly controlled, extricating the patients from the bulky battery or motion limitation. 2) The US activation also fastens the biodegradation of the device, avoiding a secondary surgical extraction and reducing the risk of infection. 3) The action of electric field and anti-mitotic drugs that concurrently targets cell cytoskeleton especially microtubule assembly and cell mitosis realize a synergistic and accumulative effect to augment cancer cell killing. The loaded chemodrug in the device is far below the effective dose of the chemodrug alone, minimizing the side effect. 4) Compared with TTField that is time-consuming, our device remarkably shortens the treatment cycle, thereby improving the patient compliance. Although some other biophysical mechanisms of electric field are still undiscovered now, it is definite that the combination of the wirelessly activated electric field and anti-mitotic drugs augments the cancer therapeutic outcome. This work not only provides new avenues for temporary IBDs, but also offers new insights into the use of wireless electric field for cancer therapy.

4. Experimental Section

This article is protected by copyright. All rights reserved.

Materials: 5,10,15,20-Tetrakis(4-aminophenyl)-21H,23H-porphine (TAPP), 2,5-Dihydroxy-terephthalaldehyde (DHPA), $Zn(NO_3)_2 \cdot 6H_2O$, paclitaxel (PTX), docetaxel (DTX) and 2-methylimidazole (2-MI) were acquired from Aladdin reagent (Shanghai) Co., Ltd. Mesitylene, methanol, anhydrous ethanol, scandium trifluoromethanesulfonate $Sc(OTf)_3$, 1,4-dioxane, tetrahydrofuran, and acetone were purchased from Shanghai McLin Biochemical Technology Co., Ltd. Polycaprolactone (PCL) was acquired from Sigma-Aldrich Inc. (St. Louis, MO). Calcein-acetoxymethyl ester (Calcein AM)/Propidium Iodide (PI) cell live/dead assay kit, Anti- β -Tubulin antibody and 3-(4,5-Dimethyl-2-Thiazolyl)-2,5-diphenyl tetrazolium bromide (MTT) were purchased from Beijing Solarbio Science & Technology Co., Ltd. Anti- γ -Tubulin monoclonal antibody, β -actin antibody and GAPDH were purchased from SAB Signalway Antibody. Fresh sheep blood was acquired from Beijing Land Bridge Technology Co., Ltd.

Preparation of ET-TENG: The contact-separation mode TENG (dimension of 1×1 cm, total thickness of ~ 130 μm) consists of two composite films. The upper composite film was fabricated by magnetron sputtering (argon flow rate of 40 sccm, 100 W, 30 min) of Mg electrode onto electrospun PCL-hCOF nanofibrous layer. The lower composite film was fabricated by magnetron sputtering of Mg electrode onto electrospun PCL nanofibrous layer.

This article is protected by copyright. All rights reserved.

The PCL layer was fabricated via electrostatic spinning (feeding rate was stabilized at 2 mL/h and voltage was constant at 15 kV) using PCL spinning solution (hexafluoroisopropanol as solvent, 5% w/v). For fabricating PCL-hCOF nanofibrous layer, hCOF (1 mg/mL) was dispersed into the PCL spinning solution. To assembly the TENG device, Mg layers of the two films were both faced upward and the peripheral area of the two composite films was integrated together by hot pressing (40 °C, 10 min), and air layer was introduced in the interior zone between the two films. Finally, CZIF-D (1 mg/mL, 80 μ L) was sprayed onto the Mg electrode surface of the TENG, denoted as ET-TENG.

Co-staining of the cells with β -tubulin and DAPI: The C6 cells were seeded in Confocal Laser Scanning Microscopy (CLSM)-exclusive culture disk (35 mm) and incubated for 24 h. After different treatments, the cells were fixed with 4% formaldehyde for 20 min, washed with PBS twice, and sealed with goat serum (1%) for 1 h. The cells were incubated with 500 μ L anti- β -Tubulin monoclonal antibody (1:1000) for 12 h, and washed with PBS twice. Next, the cells were incubated with FITC-labeled goat anti-mouse IgG (500 μ L, 1: 1000 diluted) for 2 h. DAPI (100 ng/mL) was used to stain the cell nuclei for 30 min. Finally, the cells were washed with PBS twice and observed by CLSM (Leica, SP8).

This article is protected by copyright. All rights reserved.

Western blotting: The cells after different treatments were harvested and washed twice with ice-cold Dulbecco's Phosphate-Buffered Saline (DPBS). 200 μ L CelLytic M solution containing protease inhibitors cocktail was added to lyse the cells for 15 min on a shaker at 4 °C. The lysed cells were centrifuged for 15 min at 20000 G to pellet the cell debris. Proteins were dissolved in sodium dodecyl sulfate (SDS) sample buffer containing 10% β -mercaptoethanol, separated by SDS- polyacrylamide gelelectrophoresis (PAGE) and processed for immunoblotting. Glyceraldehyde-3-phosphate dehydrogenase (GAPDH) was applied as the loading control. The used monoclonal antibodies include anti- β -actin (1:2000), anti- β -tubulin (1:2000), anti- γ -tubulin (1:2000), and anti-GAPDH (1:2000).

Cell cycle analysis: The C6 cells after different treatments were harvested through trypsinization and washed with cold Phosphate-Buffered Saline (PBS). Cold 70% ethanol was added dropwise to the cell pellet under vortexing to fix the cells at 4 °C overnight. The cells were washed with PBS twice and stained with 50 μ g/mL Propidium Iodide (PI) (including ribonuclease) at room temperature for 30 min. The samples were loaded on flow cytometer for cell cycle analysis. Data processes were carried out on Flowjo. Mitotic index was calculated as: Mitotic index = (population of mitotic cells/population of total cells) \times 100%.

This article is protected by copyright. All rights reserved.

Co-staining cells with F-actin and DAPI: C6 cells were seeded in CLSM-exclusive culture disk (35 mm) and incubated for 24 h. After different treatments, the cells were fixed with 4% formaldehyde for 20 min, washed with PBS twice. The cells were treated with 0.1% Triton X-100 in PBS for 5 minutes to increase membrane permeability, fixed with 4% formaldehyde for 20 min, and washed with PBS twice. Next, Phalloidin-iFluor™ 488 Conjugate working solution were added into the fixed cells, and incubated at room temperature for 60 minutes, washed with PBS twice. Then DAPI (100 ng/mL) was used to stain the nuclei for 30 min. Finally, the cells were washed with PBS twice and observed by CLSM.

In vivo cancer therapy: The *in vivo* anticancer effect against BALB/c nude mice with subcutaneous C6 tumors was investigated. The animal experiments were approved by the Committee on Ethics of Beijing Institute of Nanoenergy and Nanosystems (Approval Number: 2021A036). The mice were subcutaneously injected with C6 cells (5×10^5 cells suspended in 100 μ L PBS) at the subcutaneous area of the left lower abdomen. When the tumors reached ~ 100 - 200 mm^3 in volume, the mice were randomly divided into five groups (n=5): 1) control group (G1), 2) US + TENG group (G2), 3) ET-TENG group (G3), 4) DTX + US + TENG group (intratumoral injection of 5 nM DTX in PBS) (G4), and 5) US + ET-TENG group (G5). ET-TENG or TENG was surgically implanted beneath the tumor

This article is protected by copyright. All rights reserved.

tissues and the wound was subsequently sutured. After the wound was sutured for 6 h, the treatment was performed by applying US through an US probe (23 kHz, 0.8 W/cm², 90 min) directly above the tumor tissues. Ultrasonic coupling agent was used as a medium for ultrasonic conduction. Each mouse was earmarked and followed individually throughout the whole experiment. The tumor volume and body weight were recorded during the whole therapeutic course of 22 days. To comply with the animal ethics, the animals were euthanatized once the tumor tissues reached 2000 mm³.

Statistical analysis: All data are expressed as mean \pm s.d. error. Statistical differences between different groups of data were evaluated by one-way analysis of variance, and $p < 0.05$ was considered statistically significant. Asterisk (*) denotes statistical significance between bars (* $p < 0.05$, ** $p < 0.01$, and *** $p < 0.001$) conducted using GraphPad Prism 6.0 and Origin. A sample size (n) for each statistical analysis was provided in the figure legend.

Supporting Information

Supporting Information is available from the Wiley Online Library or from the author.

This article is protected by copyright. All rights reserved.

Acknowledgements

The work was supported by the National Nature Science Foundation (No. 82072065, 82202333), the Strategic Priority Research Program of the Chinese Academy of Sciences (No. XDA16021103), the Fundamental Research Funds for the Central Universities (E2EG6802X2, E2E46801), and the National Youth Talent Support Program.

Received: ((will be filled in by the editorial staff))

Revised: ((will be filled in by the editorial staff))

Published online: ((will be filled in by the editorial staff))

References

- [1] a) E. A. Foley, T. M. Kapoor, *Nat Rev Mol Cell Biol* **2013**, 14, 25; b) I. Soria-Bretones, K. L. Thu, J. Silvester, J. Cruickshank, S. El Ghamrasni, W. Ba-Alawi, G. C. Fletcher, R. Kiarash, M. J. Elliott, J. J. Chalmers, A. C. Elia, A. Cheng, A. A. N. Rose, M. R. Bray, B. Haibe-Kains, T. W. Mak, D. W. Cescon, *Sci Adv* **2022**, 8, eabq4293.
- [2] a) M. Rios Garcia, B. Meissburger, J. Chan, R. M. de Guia, F. Mattijssen, S. Roessler, A. L. Birkenfeld, N. Raschzok, F. Riols, J. Tokarz, M. Giroud, M. Gil Lozano, G. Hartleben, P. Nawroth, M. Haid, M. Lopez, S. Herzig, M. Berriel Diaz, *Adv Sci (Weinh)* **2022**, 9, e2104291; b) C. Marquis, C. L. Fonseca, K. A. Queen, L. Wood, S. E. Vandal, H. L. H. Malaby, J. E. Clayton, J. Stumpff, *Nat Commun* **2021**, 12, 1213.

This article is protected by copyright. All rights reserved.

- [3] a) S. L. Prosser, L. Pelletier, *Nat Rev Mol Cell Biol* **2017**, 18, 187; b) M. Sun, M. Jia, H. Ren, B. Yang, W. Chi, G. Xin, Q. Jiang, C. Zhang, *Nat Commun* **2021**, 12, 7157.
- [4] a) A. F. Hottinger, P. Pacheco, R. Stupp, *Neuro Oncol* **2016**, 18, 1338; b) E. J. Mun, H. M. Babiker, U. Weinberg, E. D. Kirson, D. D. Von Hoff, *Clin Cancer Res* **2018**, 24, 266; c) E. D. Kirson, V. Dbaly, F. Tovarys, J. Vymazal, J. F. Soustiel, A. Itzhaki, D. Mordechovich, S. Steinberg-Shapira, Z. Gurvich, R. Schneiderman, Y. Wasserman, M. Salzberg, B. Ryffel, D. Goldsher, E. Dekel, Y. Palti, *Proc Natl Acad Sci U S A* **2007**, 104, 10152.
- [5] a) R. Stupp, S. Taillibert, A. Kanner, W. Read, D. Steinberg, B. Lhermitte, S. Toms, A. Idbaih, M. S. Ahluwalia, K. Fink, F. Di Meco, F. Lieberman, J. J. Zhu, G. Stragliotto, D. Tran, S. Brem, A. Hottinger, E. D. Kirson, G. Lavy-Shahaf, U. Weinberg, C. Y. Kim, S. H. Paek, G. Nicholas, J. Bruna, H. Hirte, M. Weller, Y. Palti, M. E. Hegi, Z. Ram, *JAMA* **2017**, 318, 2306; b) M. J. B. Taphoorn, L. Dirven, A. A. Kanner, G. Lavy-Shahaf, U. Weinberg, S. Taillibert, S. A. Toms, J. Honnorat, T. C. Chen, J. Sroubek, C. David, A. Idbaih, J. C. Easaw, C. Y. Kim, J. Bruna, A. F. Hottinger, Y. Kew, P. Roth, R. Desai, J. L. Villano, E. D. Kirson, Z. Ram, R. Stupp, *JAMA Oncol* **2018**, 4, 495.
- [6] M. E. Lacouture, M. E. Davis, G. Elzinga, N. Butowski, D. Tran, J. L. Villano, L. DiMeglio, A. M. Davies, E. T. Wong, *Semin Oncol* **2014**, 41 Suppl 4, S1.
- [7] E. D. Kirson, Z. Gurvich, R. Schneiderman, E. Dekel, A. Itzhaki, Y. Wasserman, R. Schatzberger, Y. Palti, *Cancer Res* **2004**, 64, 3288.
- [8] a) Y. Yang, X. Hu, Y. Liu, B. Ouyang, J. Zhang, H. Jin, Z. Yu, R. Liu, Z. Li, L. Jiang, X. Lin, B. Xu, *Sci Adv* **2022**, 8, eabm5023; b) B. Chu, X. Qin, Q. Zhu, H. Wang, Z. Wen, X. Sun, Y. He, S.-T. Lee, *Nano Energy* **2022**, 100, 107471.
- [9] a) S. Yao, X. Zhao, X. Wang, T. Huang, Y. Ding, J. Zhang, Z. Zhang, Z. L. Wang, L. Li, *Adv Mater* **2022**, 34, e2109568; b) S. Yao, M. Zheng, Z. Wang, Y. Zhao, S. Wang, Z. Liu, Z. Li, Y. Guan, Z. L. Wang, L. Li, *Adv Mater* **2022**, e2205881; c) Y. Song, J. Min, Y. Yu, H. Wang, Y. Yang, H. Zhang, W. Gao, *Sci Adv* **2020**, 6; d) F.-R. Fan, Z.-Q. Tian, Z. Lin Wang, *Nano Energy* **2012**, 1, 328; e) X. Zhou, G. Li, D. Wu, H. Liang, W. Zhang, L. Zeng, Q. Zhu,

This article is protected by copyright. All rights reserved.

P. Lai, Z. Wen, C. Yang, Y. Pan, Exploration **2023**, DOI: 10.1002/EXP.20220090; f) I. M. Imani, B. Kim, X. Xiao, N. Rubab, B. J. Park, Y. J. Kim, P. Zhao, M. Kang, S. W. Kim, Adv Sci (Weinh) **2023**, 10, e2204801.

[10]a) Q. Zheng, B. Shi, F. Fan, X. Wang, L. Yan, W. Yuan, S. Wang, H. Liu, Z. Li, Z. L. Wang, Adv Mater **2014**, 26, 5851; b) H. Ouyang, Z. Liu, N. Li, B. Shi, Y. Zou, F. Xie, Y. Ma, Z. Li, H. Li, Q. Zheng, X. Qu, Y. Fan, Z. L. Wang, H. Zhang, Z. Li, Nat Commun **2019**, 10, 1821.

[11]a) Y. Jiang, K. Dong, X. Li, J. An, D. Wu, X. Peng, J. Yi, C. Ning, R. Cheng, P. Yu, Z. L. Wang, Advanced Functional Materials **2020**, 31, 2005584; b) L. Lan, J. Xiong, D. Gao, Y. Li, J. Chen, J. Lv, J. Ping, Y. Ying, P. S. Lee, ACS Nano **2021**, 15, 5307.

[12]a) Q. Zheng, Y. Zou, Y. Zhang, Z. Liu, B. Shi, X. Wang, Y. Jin, H. Ouyang, Z. Li, Z. L. Wang, Sci Adv **2016**, 2, e1501478; b) R. Pan, W. Xuan, J. Chen, S. Dong, H. Jin, X. Wang, H. Li, J. Luo, Nano Energy **2018**, 45, 193; c) D. M. Lee, N. Rubab, I. Hyun, W. Kang, Y. J. Kim, M. Kang, B. O. Choi, S. W. Kim, Sci Adv **2022**, 8, eabl8423.

[13]a) Y. Xi, J. Ge, M. Wang, M. Chen, W. Niu, W. Cheng, Y. Xue, C. Lin, B. Lei, ACS Nano **2020**, 14, 2904; b) X. Ji, D. Guo, J. Ma, M. Yin, Y. Yu, C. Liu, Y. Zhou, J. Sun, Q. Li, N. Chen, C. Fan, H. Song, Adv Mater **2021**, 33, e2100949; c) J. Lee, H. R. Cho, G. D. Cha, H. Seo, S. Lee, C. K. Park, J. W. Kim, S. Qiao, L. Wang, D. Kang, T. Kang, T. Ichikawa, J. Kim, H. Lee, W. Lee, S. Kim, S. T. Lee, N. Lu, T. Hyeon, S. H. Choi, D. H. Kim, Nat Commun **2019**, 10, 5205.

[14]R. Hinchet, H. J. Yoon, H. Ryu, M. K. Kim, E. K. Choi, D. S. Kim, S. W. Kim, Science **2019**, 365, 491.

[15]S. Yao, M. Zheng, S. Wang, T. Huang, Z. Wang, Y. Zhao, W. Yuan, Z. Li, Z. L. Wang, L. Li, Advanced Functional Materials **2022**, 2209142.

[16]R. Feiner, L. Engel, S. Fleischer, M. Malki, I. Gal, A. Shapira, Y. Shacham-Diamand, T. Dvir, Nat Mater **2016**, 15, 679.

This article is protected by copyright. All rights reserved.

-
- [17] M. Dogterom, G. H. Koenderink, *Nat Rev Mol Cell Biol* **2019**, 20, 38.
- [18] M. Preciado Lopez, F. Huber, I. Grigoriev, M. O. Steinmetz, A. Akhmanova, G. H. Koenderink, M. Dogterom, *Nat Commun* **2014**, 5, 4778.
- [19] Q. Zhou, Z. Hou, S. Zuo, X. Zhou, Y. Feng, Y. Sun, X. Yuan, *Cancer Sci* **2019**, 110, 1194.
- [20] S. Huo, P. Zhao, Z. Shi, M. Zou, X. Yang, E. Warszawik, M. Loznik, R. Gostl, A. Herrmann, *Nat Chem* **2021**, 13, 131.

This article is protected by copyright. All rights reserved.

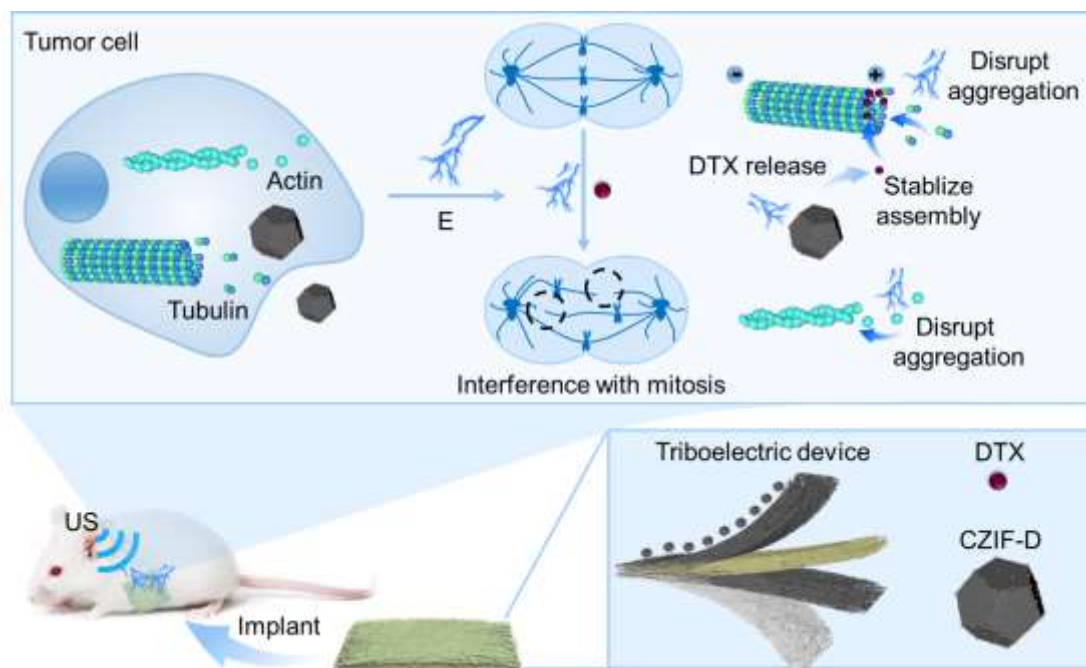
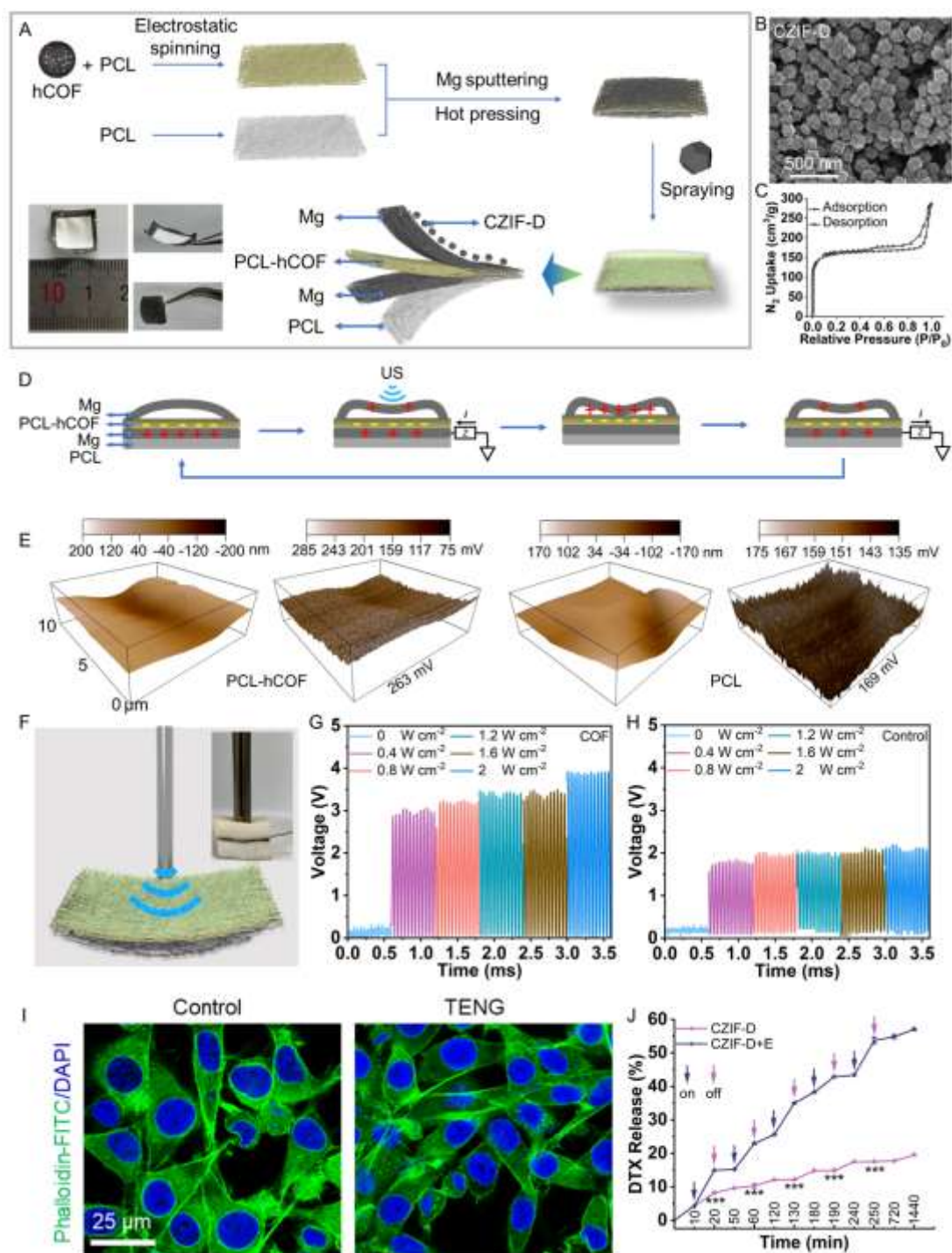


Figure 1. Schematic diagram of cancer therapy with the US-driven wireless ET-TENG.

Electrostimulation (E) and Ultrasound (US).

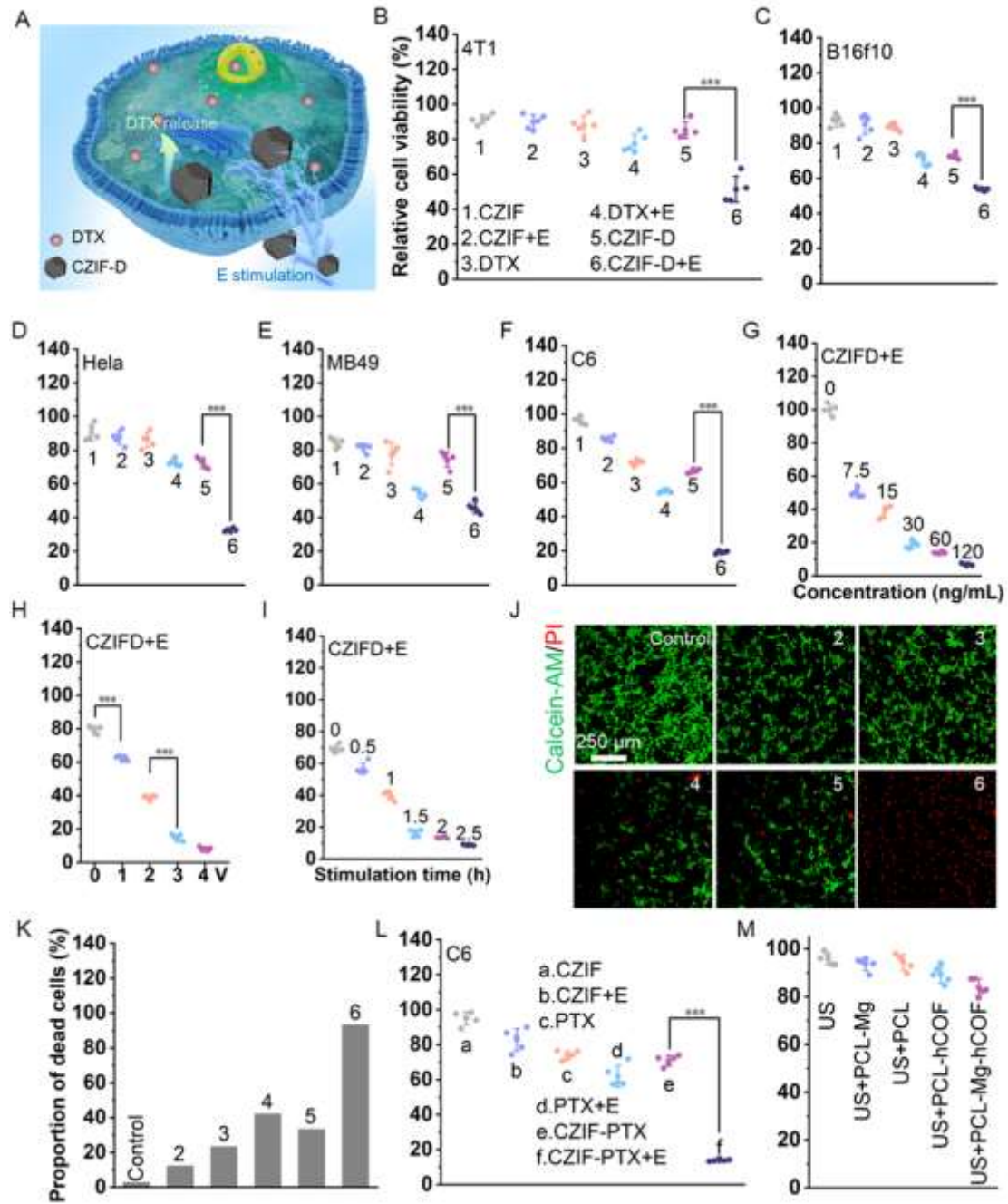
This article is protected by copyright. All rights reserved.



This article is protected by copyright. All rights reserved.

Figure 2. Preparation, output performance, and biocompatibility of ET-TENG. A) Schematic illustration of the detailed structure and photographs of ET-TENG. B) SEM image of CZIF-D. C) N₂ adsorption-desorption isotherms of CZIF at 77 K. D) A cycle of electricity generation process of ET-TENG under ultrasonic mechanical waves. E) KPFM images showing the surface potential of PCL and PCL-hCOF. F) Schematic illustration of US-activated electric output of ET-TENG between two pieces of pork skins. The inset is optical photograph of the experimental setup. G) Voltage outputs of ET-TENG prepared with the PCL-hCOF film as the triboelectric layer at different ultrasonic powers. H) Voltages output of ET-TENG prepared with the pure PCL film as the triboelectric layer at different ultrasonic powers. I) L929 cells stained by phalloidin-FITC and DAPI after treatment with TENG for 24 h. J) Drug release of DTX with or without the E (n=3, mean \pm SD), ***p < 0.001.

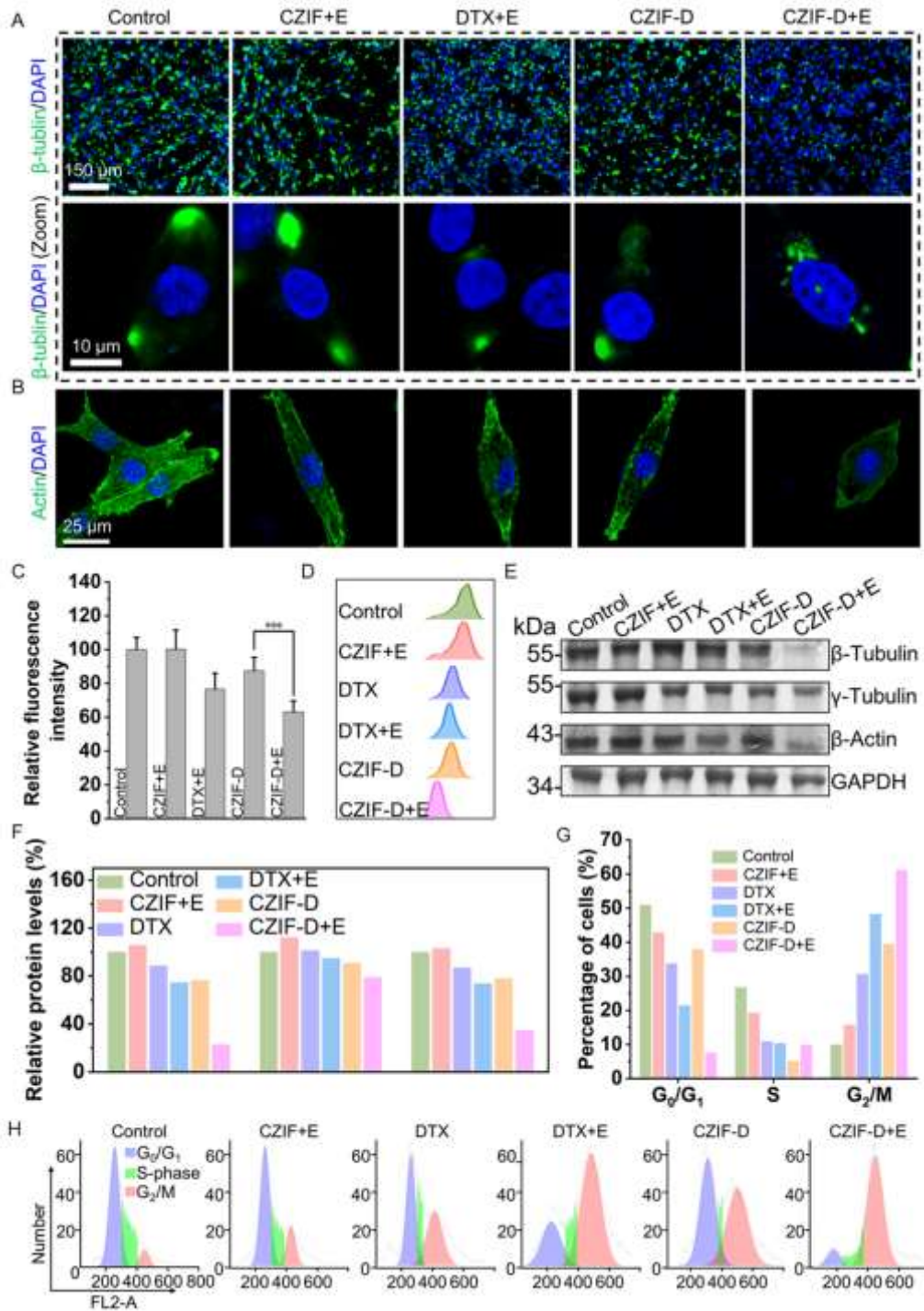
This article is protected by copyright. All rights reserved.



This article is protected by copyright. All rights reserved.

Figure 3. Cancer therapeutic effect of ET-TENG at the cell level. A) Schematic illustration of the E-promoted therapy with CZIF-D. Viability of B) 4T1, C) B16f10, D) Hela, E) MB49 and F) C6 cells at 24 h additional culture after different treatments (n=5, mean \pm SD). G-I) Viability of C6 cells after CZIF-D + E treatment at different G) CZIF-D concentrations, H) electrical voltages and I) E stimulation durations (n=5, mean \pm SD). J) C6 cells co-stained with Calcein-AM (green fluorescence) and PI (red fluorescence) and K) corresponding statistic result of the percent of dead cells. L-M) Viability of C6 cells at 24 h additional culture after different treatments (n=5, mean \pm SD), ***p < 0.001.

This article is protected by copyright. All rights reserved.



This article is protected by copyright. All rights reserved.

Figure 4. Interference of cell cytoskeleton and influence on cell cycle in C6 cells. A) Immunofluorescence images of β -tubulin in C6 cells after different treatments. The zoom part shows the aggregation of β -tubulin within individual cells. B) Immunofluorescence images of F-actin assembly in C6 cells after different treatments. The cell nuclei were stained with 4',6-diamidino-2-phenylindole (DAPI) in A-B. C) Statistic result shows the relative mean fluorescence intensity of β -tubulin in A. Fluorescence in the control group is set as 100 ($n=6$, mean \pm SD). D) Flow cytometry analysis of β -tubulin in C6 cells after different treatments. E) Western blot analysis of β -tubulin, γ -tubulin and β -actin expression in C6 cells upon different treatments. Glyceraldehyde-3-phosphate dehydrogenase (GAPDH) serves as a loading control. F) Relative protein levels of β - tubulin, γ -tubulin and β -actin after normalization treatment. G) Cell cycle analysis after different treatments and H) corresponding cell cycle distribution expressed as percentages, *** $p < 0.001$.

This article is protected by copyright. All rights reserved.

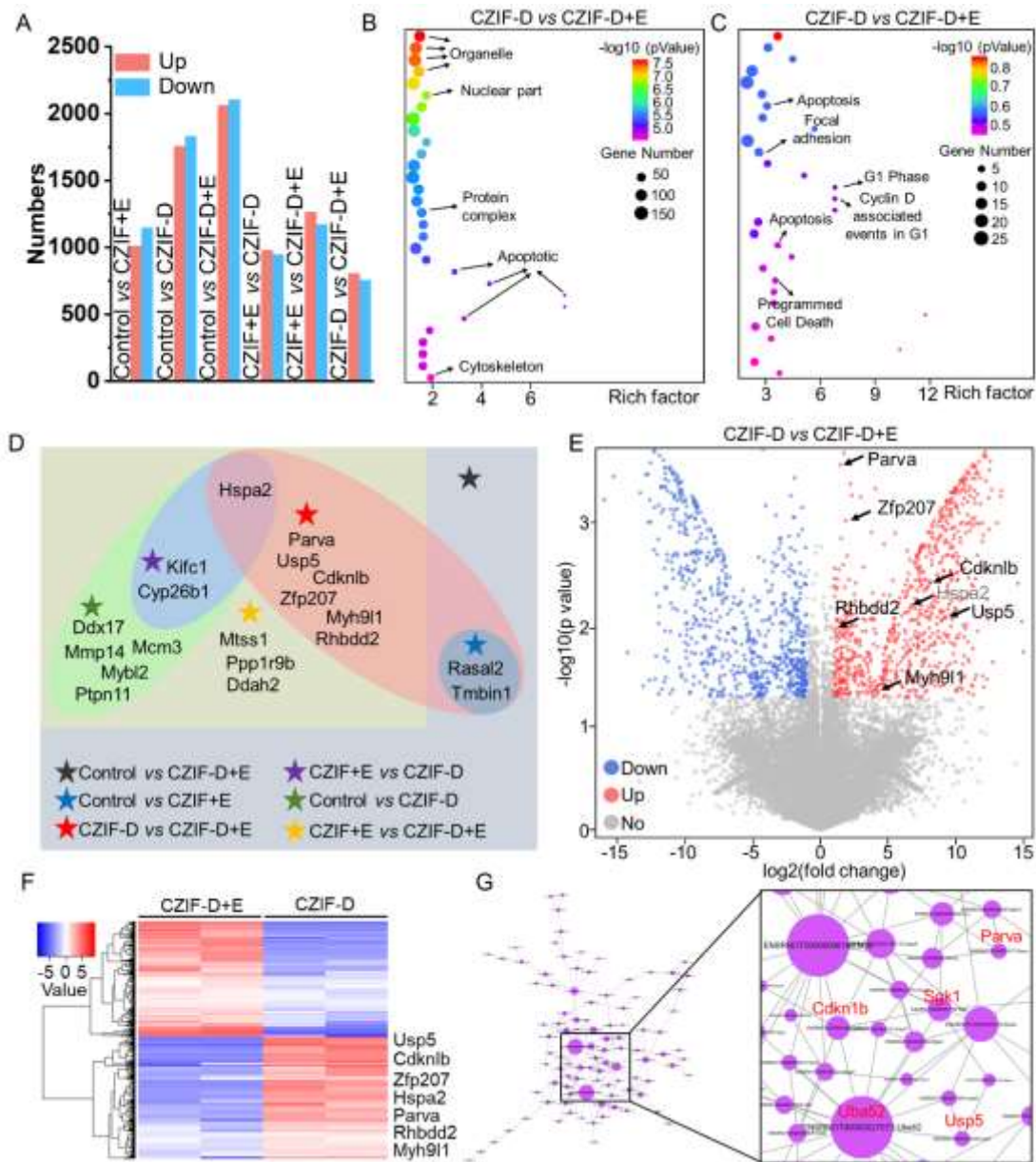
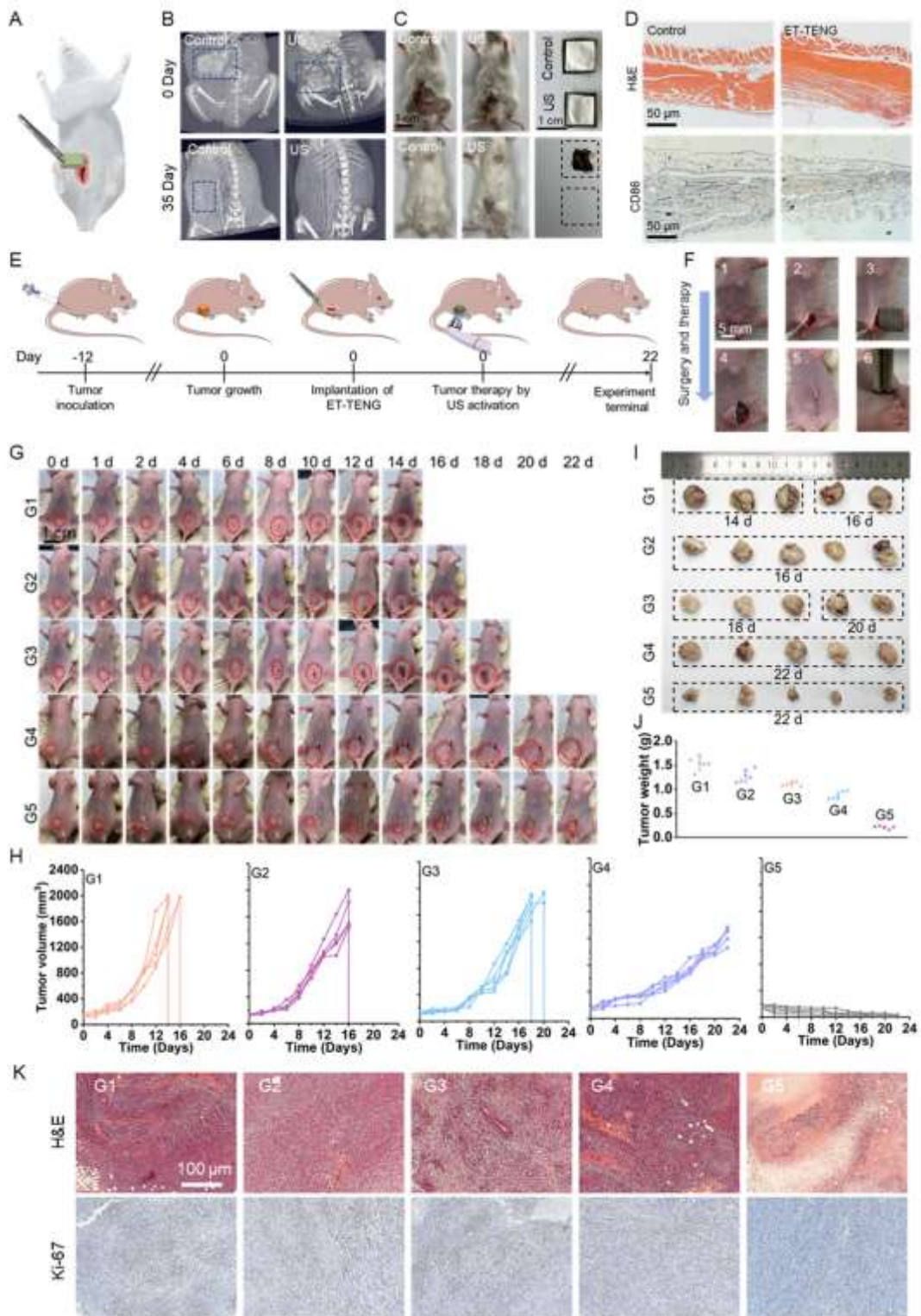


Figure 5. Bulk RNA-sequencing analysis results. A) The number of differentially expressed genes (DEGs) of C6 cells after different treatments. B) Gene Ontology (GO) term enrichment analysis of DEGs after the CZIF-D + E treatment compared with the CZIF-D treatment. C) KEGG pathway enrichment analysis after the CZIF-D + E treatment compared with the

This article is protected by copyright. All rights reserved.

CZIF-D treatment. D) The regulated expression of mitosis-related genes between different groups. E) Volcano plots of DEGs after the CZIF-D and CZIF-D + E treatments. F) Hierarchical clustering analysis of DEGs after the CZIF-D + E treatment. Red and blue colors represent upregulated and downregulated genes, respectively. Key DEGs are listed on the right. G) DAG of each GO category for differential genes upon the treatment of CZIF-D + E.

This article is protected by copyright. All rights reserved.



This article is protected by copyright. All rights reserved.

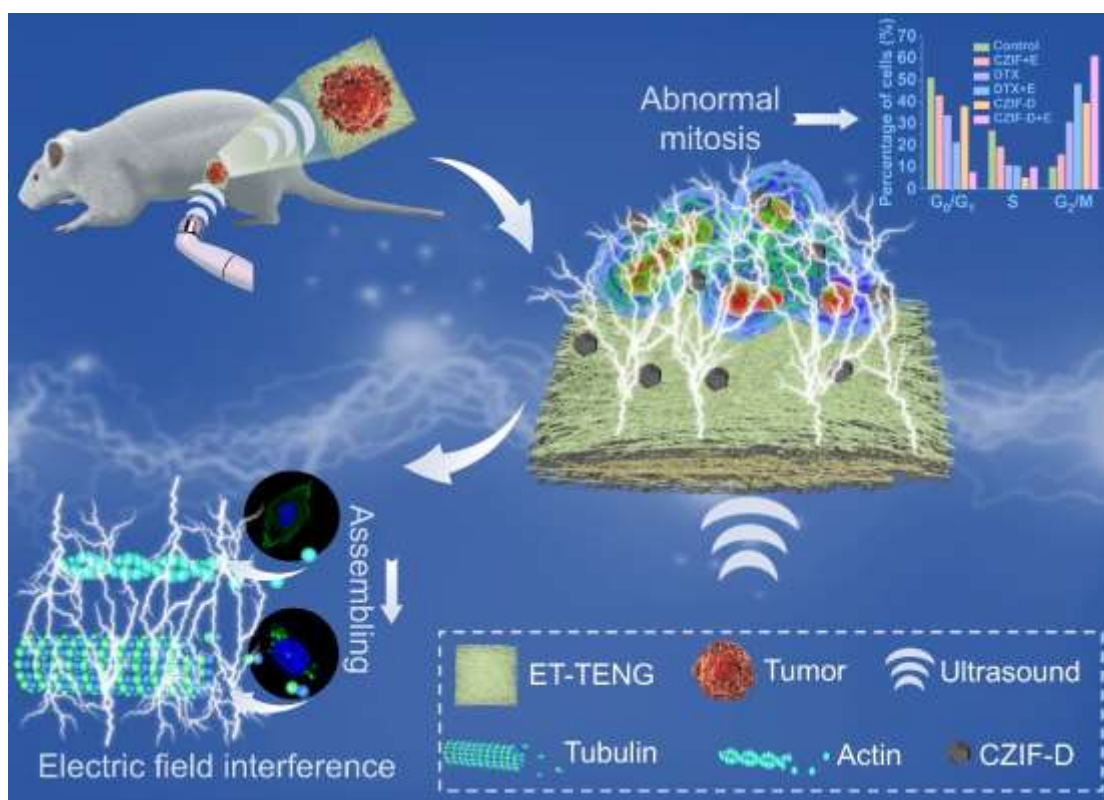
Figure 6. *In vivo* implantation, biodegradability and cancer therapy of ET-TENG. A) Schematic diagram of the *in vivo* implantation of ET-TENG in mice. B) Micro-CT imaging of the mice before and after 35 days of subcutaneous implantation of ET-TENG with and without US activation. C) Optical photographs of the devices and the mice before and after 35 days of implantation. D) H&E and CD86 staining of the tissues at the device implantation site after 35 days of implantation. E) Schematic illustration of the cancer therapy with TE-TENG. F) 1-6 represent optical images of the *in vivo* implantation and treatment process of ET-TENG. G) Photographs of the stripped tumor tissues at the terminal of the therapy. H) Tumor volume change of the mice during the treatment. I) Photographs of representative mice in different groups during the 22-days of treatment. Dashed boxes and labeled point-in-times indicate the moments when tumors were taken, temporarily preserved, and photographed on Day 22 together. J) Mean tumor weights after the excision on day 22 (n=5, mean \pm SD). K) H&E and Ki-67 staining of the tumor tissues. Control group (G1), US + TENG group (G2), ET-TENG group (G3), DTX + US + TENG group (G4) and US + ET-TENG group (G5).

In this work, we develop an implantable, biodegradable, and wireless triboelectric device for cancer therapy. Next, we demonstrate the significantly enhanced tumor therapeutic effects against a broad-spectrum of tumors through cell and animal experiments.

Shuncheng Yao, Shaobo Wang, Minjia Zheng, Zhuo Wang, Zhirong Liu, Zhong Lin Wang^{*}, Linlin Li^{*}

Implantable, Biodegradable, and Wireless Triboelectric Devices for Cancer Therapy Through Disrupting Microtubule and Actins Dynamics

This article is protected by copyright. All rights reserved.



This article is protected by copyright. All rights reserved.